Nonlinear analytical modeling of mass-timber buildings with post-tensioned rocking walls

Nonlinear Analytical Modeling of Mass-Timber Buildings with Post-Tensioned Rocking Walls

Angelo Aloisio[1*], Marco Martino Rosso[2], Da Huang[3], Asif Iqbal[4], Massimo Fragiacomo[1] and Shiling Pei[3]

[1*]Civil Environmental and Architectural Engineering Department, Universit degli Studi dell'Aquila, via Giovanni Gronchi n.18, L'Aquila, 67100, Italy.
[2]DISEG, Department of Structural, Geotechnical and Building Engineering, Politecnico di Torino, Corso Duca Degli Abruzzi, 24, Turin, 10128, Italy.
[3]Faculty of Civil and Environmental Engineering, Colorado School of Mines, 1500 Illinois St, Golden, 80401, Colorado, USA.
[4]School of Engineering, University of Northern British Columbia, 3333 University Way, Prince George, British Columbia, V2N 4Z9, Canada.

*Corresponding author(s). E-mail(s): angelo.aloisio1@univaq.it;
Contributing authors: marco.rosso@polito.it;
huang@mymail.mines.edu; asif.iqbal@unbc.ca;
massimo.fragiacomo@univaq.it; spei@mines.edu;

Abstract

The dynamic response of post-tensioned rocking walls in a mass timber building can be reduced to a single-degree-of-freedom (SDOF) model. In this model, the rocking wall panel is simplified as a rigid block, while the base rotation represents the degree of freedom of the entire structure. The paper presents an analytical approach to develop and calibrate this nonlinear model using shake table tests of a full-scale two-story building with CLT rocking walls. The experimental data are used to estimate the parameters of the governing equation using least-squares optimization. The correlation between the obtained parameters and the

cumulative dissipated energy led to a nonlinear model with degradation behavior captured. After that, the calibrated model was used to assess the fragility functions of the structure under repetitive seismic events.

Keywords: cross-laminated timber, post-tensioned rocking wall, experimental investigation, non-linear dynamic analysis, fragility curve

1 Introduction

Traditional wood structures are prone to exhibit a significant reduction of the structural capacity after the repetition of seismic events [1–3]. Many traditional wood buildings derive from the assemblage of timber elements with metal connectors, representing the primary source of energy dissipation during seismic events. The damage of the connections is irreversible and significantly compromises the quick recovery after the event [4–6]. Furthermore, the plasticization of the connector causes the local plasticization of the timber fibres, determining an evident reduction of the structural capacity after the event [7]. Among engineered-wood solutions, cross-laminated timber (CLT) is growing as a practical, constructive choice in seismic prone areas, especially in tall timber buildings [8]. Compared to light-frame buildings, CLT structures have high in-plane stiffness and a significant load-carrying capacity; The main features of CLT building depend on the physical parameters of the timber panels and the mechanical properties of the connections used (hold-downs and angle brackets, more robust and stiffer than the connectors used in lightweight structures) [9–11]. However, although panelized CLT structures exhibit higher resistance and ductility than lightweight timber structures, they can experience significant damage during an earthquake that is hard to repair [12–14]. After a seismic event, the extensive damage related to the plasticization of the connections and local damage of timber entails the demolition and reconstruction of the building rather than a quick recovery obtained by a targeted replacement of a few structural components [15]. Damage to traditional wood frame building is represented as pinching in their hysteretic loops. Pinching manifests in a reduced stiffness of the re-loading paths of the hysteretic response [16–18]. In timber connections, the first-loading path depletes most of the dissipation capacity. The re-loading paths manifest an opposite curvature to the first loading ones and are associated with minimal energy dissipation [19, 20]. According to many scholars, pinching represents the primary weakness of timber structures [21, 22]. Therefore, many scientists attempted to enhance the resilience of timber structures by reducing or eliminating pinching [23–25]. Dissipation devices, added as coupling elements between timber shear walls, increase the dissipation capacity due to the sole connections, reducing the consequences of pinching [26–30]. This solution does not eliminate pinching but enhances the structural dissipation sources. Other scholars

attempted to eliminate pinching by developing pinching-free connections [31–37]. This solution improves the cyclic behaviour significantly, as demonstrated from multiple experimental tests [38–40]: the mutual sliding between metal plates with interposed shim material guarantees an almost Coulomb-like dissipation [41]. Aside from pinching-free connections and friction-based devices, post-tensioned CLT rocking walls coupled with steel energy dissipators also can achieve a significant reduction of pinching and enhancement of structural resilience [42–45]. These resilient wood lateral force-resisting systems were initially proposed and studied by researchers in New Zealand in the early 2000s [46, 47]. Post-tensioning techniques have been applied to wood-frame moment connections and walls [48–51] and used in real building projects [52]. The subsequent development of the post-tensioned wood system led to the commercial application of such techniques in building projects [53]. Recently, a reversed cyclic load testing of post-tensioned CLT rocking walls was conducted by [54] and modelling parameters were derived from that data by [55]. There are also recent studies on the time-dependent performance of post-tensioned CLT walls [56–58]. A six-university collaborative research project called the Natural Hazards Engineering Research Infrastructure (NHERI) Tall Wood Project funded by the National Science Foundation (NSF) aims to develop a resilience-based seismic design methodology for tall wood buildings. In 2017, Pei et al. [59] carried out shake table tests of a two-story mass timber building with post-tensioned cables and U-shaped steel dissipators. So far, a few modelling attempts aimed at estimating the response of mass-timber structures with CLT rocking walls using analytical modelling [27, 38, 60–62]. Pei et al. [63, 64] proposed a computationally efficient numerical model for predicting seismic responses of post-tensioned cross-laminated timber (CLT) rocking wall systems. The rocking wall is modelled as a simple linear beam element with a nonlinear rotational spring at the base. In this paper, the authors further investigate the experimental seismic response of the full-scale two-story mass timber building with generalization of the model proposed in [63], but with further reduced number of degrees of freedom and simplified kinematic hypotheses. The model was reduced to the equation of motion for a Single-Degree-of-Freedom (SDOF) oscillator that can accurately capture the dynamic response reflected in the experimental data. The equation, obtained from the principle of virtual works in linear dynamics, proved to effectively represent the building response in terms of base rotation of the CLT wall. The main advantage of the proposed model compared to the one by [63] is the analytical formulation based on elementary governing equations. This model can be easily used for extensive parametric analysis and design purposes without needing FE formulations. Lastly, the fragility curves are obtained from Truncated Incremental Dynamic Analysis.

2 Mechanical model of a structure with rocking post-tensioned wall

Under specific kinematic assumptions, the mechanical model of a frame structure coupled with a rocking wall behaves like an SDOF oscillator. In this section, the authors will demonstrate this observation by deriving the equation of motion of a mechanical model possibly representative of the full-scale two-story mass timber building with post-tensioned rocking CLT walls tested in 2017 at the NHERI@UCSD large outdoor shake table facility. Fig.1 represents the chosen simplified mechanical model of the two-story building. The model consists of a shear-type two-story frame with lumped masses and two rocking walls. The columns and the rocking walls have no mass, and the total mass is lumped in the storeys. The symmetry of both the tested structure and the excitation supported the development of a planar model, neglecting the 3-d effects. The two rocking walls are mutually connected by equivalent shear springs representatives of the UFP steel dissipators. The rocking walls are connected to the frame by sliding constraints. The shear transfer detail devised by [59] releases vertical constrain and allows the sliding between the CLT wall and each story. Each rocking wall possesses a pivot point by one edge of the panel due to the geometrical configuration of the building. The rocking walls are inside the building, and both connected to the storeys. This configuration leads to the identity of displacement between the two rocking walls and the storeys. Unbonded prestressed steel cables connected to the foundation stabilize the rocking motion of the CLT walls. The model neglects the stiffness of the sliding constraints at the base of the CLT panels.

Two variables describe the kinematic response of the mechanical system: the

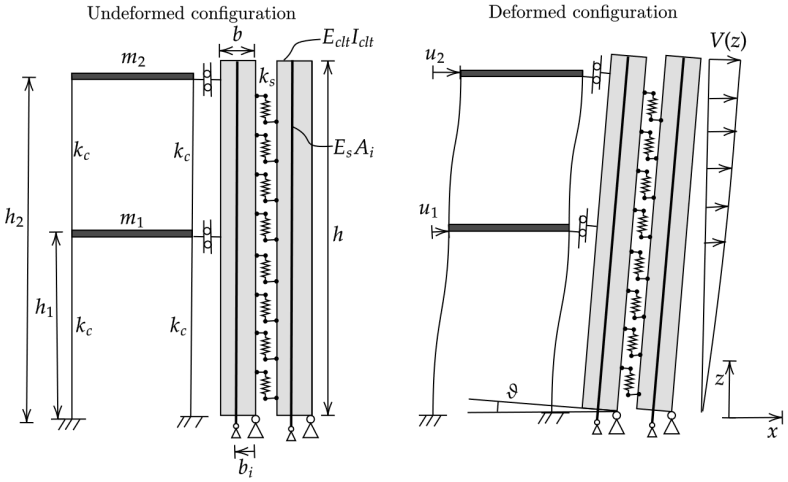

Fig. 1 Mechanical model of a 2-story frame coupled with a rocking wall.

rigid rotation of the CLT panels (θ) and the horizontal displacement field of the CLT panel due to elastic deformation ($v(z)$), where z spans the CLT panel length. The displacement field of the rocking walls is the summation of the rigid and deformation contributions, as shown in Eq.1:

$$u(z) = V(z) + \theta z; \quad v(x) = \theta x \tag{1}$$

The following equations express the horizontal constraint between the rocking walls and the frame :

$$u_1 = u(h_1); \quad u_2 = u(h_2) \tag{2}$$

where u_1 and u_2 are the horizontal displacements of the two storeys. The current model represents a possible enhancement of the model proposed by [63]. The main differences between this model and the one by [63] are:

- This model does not include the stiffening and dissipative contribution of the rocking walls into the equivalent stiffness of a lumped-mass shear-type frame model. The current model represents the rocking walls and the shear-type frame separately, each described by its kinematic variables.
- As a consequence of the previous point, this model does not divide the CLT wall into a sequence of segments, each one corresponding to the rocking wall comprised of two storeys. Instead, the CLT wall is modelled as a continuum and has the same displacement and rotation at each storey. Consequently, this model respects the continuity of rotation between segments of the CLT wall, neglected in the frame model, and includes the CLT deformability without segmenting the wall stiffness in the summation of cantilevered-like beam elements.
- This model does not explicitly account for the stiffness of the angle brackets connecting the wall to the foundation. The sliding is eliminated by considering a fixed pivot point.
- The model is derived under the assumption of small rotations and displacements. The maximum rotation values of the CLT panel are lower than 0.1. Therefore, the inclusion of the nonlinear terms considered by the Housner nonlinear block model [65] is unnecessary for engineering purposes.
- The model neglects the dissipative contribution of impact in the rocking motion [66, 67]. Dissipation mostly depends on the UFP dissipators.
- The main advantage of the proposed model compared to the one by [63] is the analytical formulation based on elementary governing equations. This model can be easily used for extensive parametric analysis and design purposes without needing FE solutors.

The equations of motion are derived from the Theorem of Virtual Works by minimizing the total energy of the mechanical system. There are three energy sources related to the action of elastic, inertial and external forces. The summation of the virtual works $\mathcal{W}$ associated with the action of the three force typologies is zero:

$$\mathcal{W}_{elastic} + \mathcal{W}_{inertial} + \mathcal{W}_{external} = 0 \tag{3}$$

In the following paragraphs, the authors will explicit the virtual work made by the elastic, inertial an external forces, labelled $\mathcal{W}_{elastic}$, $\mathcal{W}_{inertial}$ and $\mathcal{W}_{external}$ respectively.

2.1 Elastic forces

The virtual work done by the elastic forces is the summation of the following addends:

$$\mathcal{W}_{elastic} = \mathcal{W}_{\text{CLT}} + \mathcal{W}_{\text{UFP}} + \mathcal{W}_{tendons} + \mathcal{W}_{columns} \tag{4}$$

where $\mathcal{W}_{\text{CLT}}$, $\mathcal{W}_{\text{UFP}}$, $\mathcal{W}_{tendons}$ and $\mathcal{W}_{columns}$ are the virtual works done by the CLT internal stresses, the UFP resisting forces, the tendons stress and the columns internal forces, respectively.
Initially, the authors assumed that the CLT panel behaves like an equivalent Euler-Bernoulli beam. The equivalent beam has null horizontal displacement and bending moment at the base. The pivot point is fixed and does not allow sliding motions ($V(0) = 0$), while the steel tendons are connected to the foundation and do not provide a bending constraint at the panel base ($V''(0)$). The CLT panel has a free end, associated with null shear forces ($V'''(h) = 0$) and bending moment ($V''(h) = 0$). The considered constraint conditions of the CLT panel lead to a null displacement field and consequently to a null virtual work ($\mathcal{W}_{\text{CLT}} = 0$). Straightforward analytical derivation can prove that a mass-less wall does not deform under the considered constraint conditions. This evidence led to the assumption of a rigid-like behaviour of the CLT wall, as anticipated in the introduction. The CLT panel does not deform and behaves like a rigid block, whose motion is described by the θ variable. Accordingly, the virtual work associated with the elastic forces reduces to the summation of the UFP dissipators, the tendons and the columns. Therefore, the following equation holds:

$$\begin{aligned}\mathcal{W}_{elastic} =& \mathcal{W}_{\text{UFP}} + \mathcal{W}_{tendons} + \mathcal{W}_{columns} = \\ =& \theta \left[+n_s k_s b^2 + \sum_{i=1}^{n} \left(\frac{N_0}{\theta} + E_s A_i \frac{b_i}{h} \right) \frac{b_i}{h_i} + k_1 h_1^2 + k_2 (h_2 - h_1)^2 \right] \delta\theta\end{aligned} \tag{5}$$

where θ is the base rotation, n_s the number of UFP dissipators, k_s the stiffness of the UFP dissipators, n the number of tendons, N_0 the tendon prestressing force, E_s and A_i the elastic modulus and cross-section area of the i-th tendons, b_i the distance between the pivot point and the i-th tendon, h the height of the CLT panel, k_1 and h_1 the horizontal stiffness and the height of the first storey, k_2 and h_2 the horizontal stiffness and the height of the second storey.
The absence of the CLT panel deformation reduces the degrees of freedom of the mechanical system to the sole base rotation θ. Interestingly, the coupling of a two-degrees of freedom system, a two-story frame, with an internal rocking

wall causes the degrees of freedom condensation. This phenomenon does not happen in case of rocking walls coupled with linear or nonlinear devices to the building story's. In that case, the mechanical system possess more degrees of freedom, as demonstrated by [67, 68].

2.2 Inertial and external forces

The virtual work of the inertial forces is associated with the storeys contributions:

$$\begin{aligned}\mathcal{W}_{inertial} =& \mathcal{W}_{\text{1st-storey}} + \mathcal{W}_{\text{2nd-storey}} = \\ =& m_1 \left(\ddot{u}_1 + \ddot{u}_g\right) \delta u_1 + m_2 \left(\ddot{u}_2 + \ddot{u}_g\right) \delta u_2 = \\ =& \left\{ \left[m_1 \left(h_1 \ddot{\theta}_1 + \ddot{u}_g \right) \right] h_1 + \left[m_2 \left(h_2 \ddot{\theta} + \ddot{u}_g \right) \right] h_2 \right\} \delta\theta\end{aligned} \tag{6}$$

where $\ddot{*}$ indicates the double time derivative, u_1 and u_2 are the horizontal displacements of the first and second storey respectively, and $\ddot{u}_g$ is the ground excitation in terms of acceleration. The two displacements are expressed as function of the base rotation.
The virtual work done by external forces is null, because there are no external forces acting on the structure.

$$\mathcal{W}_{external} = 0 \tag{7}$$

2.3 Governing equations

The summation of Eq.6 and Eq.5 leads to the equation of the SDOF system representative of the mechanical model in Fig.1:

$$I_\theta \ddot{\theta} + K_\theta \theta = -S_x \ddot{u}_g \tag{8}$$

$$I_\theta = m_1 h_1^2 + m_2 h_2^2 \tag{9}$$

$$K_\theta = n_s k_s b^2 + \sum_{i=1}^{n} \left(N_0 + E_s A_i \frac{b_i}{h} \right) b_i + k_1 h_1^2 + k_2 (h_2 - h_1)^2 \tag{10}$$

$$S_x = m_1 h_1 + m_2 h_2 \tag{11}$$

where I_θ is the rotational inertia of the storey masses, K_θ is an equivalent rotational spring and S_x is the expression of the static moment.
Eq.8 describes the dynamics of the mechanical system in Fig.1 in linear elasticity, without dissipation. The next paragraphs will discuss the modelling choices of dissipation by including an equivalent viscous term.

3 Test description

This paper utilizes the response of a full-scale two-story mass timber building with post-tensioned rocking CLT walls for model calibration. The authors

present a few details of the tested building, significant for the current research, before discussing the building dynamics and deriving the equation of motion. Complete details of the building and the tests are in [59]. The building was tested in 2017 at the NHERI@UCSD large outdoor shake table facility. Fig.2 shows the two-story building and a schematic detail of the post-tensioned rocking walls. The building is symmetric and tested using a uniaxial shake table.

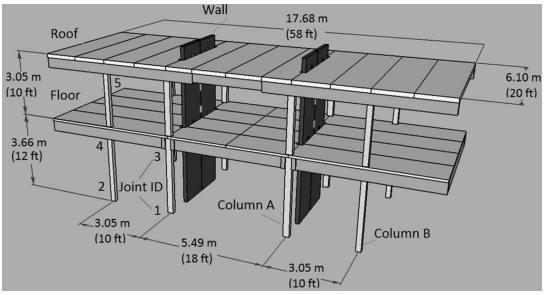

(a)

(b)

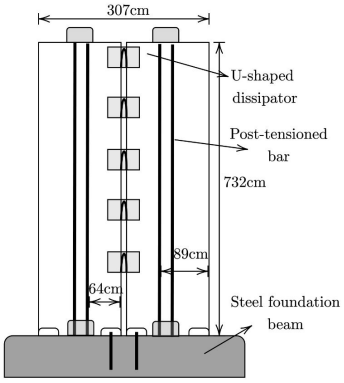

(c)

Fig. 2 Test building configuration: (a) solid model and dimensions; (b) photo of the constructed building and (c) schematic drawing of the rocking CLT wall.

There were two sets of coupled CLT rocking walls installed in the test specimen, as shown in Fig.2. The walls were coupled using U-shaped flexural steel plate (UFP) energy dissipators, analogue to the ones tested by [69]. Each panel had four external post-tensioned steel rods placed symmetrically near the centre of the wall panel (two on each side). A steel saddle detail, installed on the top of the panel, anchored the post-tensioned rods. The rocking-wall lateral system was connected to the diaphragm using constructive details, which allow the uplift of the wall panel and provide out-of-plane bracing of the wall. A dowel-type steel shear key, inserted into a vertically slotted hole, allowed unconstrained uplift of the rocking wall while transferring lateral loads. The main objective of the testing program was to validate the resilient performance

of the post-tensioned CLT rocking-wall lateral system at different levels of seismic intensity. The test building was subjected to a total of 14 earthquake excitations selected to represent three hazard levels for a site near Seattle (USA).

4 Discussion of the modelling choices and estimation of the system nonlinearity

The mechanical model in Eq.8 is straightforward, reducing a complex 3-d building into an equivalent SDOF system. In this section, the authors discuss the modelling choices by presenting selected results of the test data:

- The measured base rotation of the CLT panel is compared to the rotation of the storeys with respect to the pivot point (Subsec. Base rotation);
- The Fast-Fourier-Transform of the measured base rotation (Subsec. Fast-Fourier-Transform);
- The spectrogram of measured base rotation with indication of the frequency ridge with highest energy content (Subsec. Spectrogram);
- The experimental force-displacement plots (Subsec. Hysteresis curve);

4.1 Base rotation

The authors prove that the base rotation is the prevalent degree of freedom of the structural system by comparing three measured parameters:

$$\theta, \frac{u_1}{h_1}, \frac{u_2}{h_2} \tag{12}$$

Fig.3 superposes the three measured variables θ, $\frac{u_1}{h_1}$, and $\frac{u_2}{h_2}$ in each of the 14 tests. If θ is the structural degree of freedom, u_1 and u_2 can be written in terms of base rotation $\theta = \frac{u_1}{h_1} = \frac{u_2}{h_2}$.

Fig.3 plots the three measured variables, θ, u_1/θ and u_2/θ for each of the 14 shake table tests. Despite higher discrepancies in Test No 3,4, and 5, there is a substantial coincidence between the three variables, proving that θ is the prevalent degree of freedom of the two-storey building. Additionally, the plots show that a very low rotation amplitude distinguishes the rocking motion. This fact endorses the adoption of the linear model in Eq.8 and the consequent neglection of the nonlinear contributions typical of high-amplitude rocking motions. Tab.1 reports the Root Mean Square Error estimated between the first story rotation (u_1/h_1) and the CLT wall base rotation (θ), and second story rotation (u_2/h_2) and the CLT wall base rotation (θ). The RMSE is minimal and further proves the significant agreement between the three variables. The horizontal displacements of the storeys are not independent, but related by the kinematic equations in Eq.1.

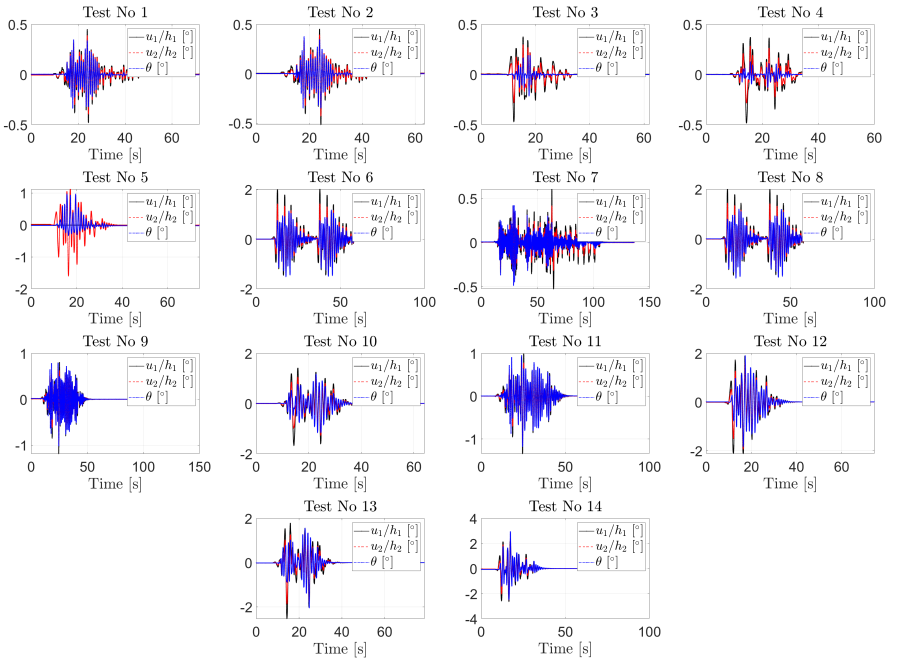

Fig. 3 Comparison between three different estimates of the base rotation, from the first (u_1/h_1) and second story (u_2/h_2) displacement and from the CLT wall uplift (θ).

Table 1 Relative difference between the maximum of the first ($u_{1,\max}/h_1$) and second story rotation ($u_{2,\max}/h_2$) and the maximum of the CLT wall base rotation ($\theta_{\max}$) in %.

Test No	$(\frac{u_{1,\max}}{h_1} - \frac{u_{2,\max}}{h_2})/\frac{u_{1,\max}}{h_1}$	$(\frac{u_{1,\max}}{h_1} - \theta_{\max})/\frac{u_{1,\max}}{h_1}$	$(\frac{u_{2,\max}}{h_2} - \theta_{\max})/\frac{u_{2,\max}}{h_2}$
1	-18.09	-33.68	-15.59
2	-17.42	-32.98	-15.56
3	-40.76	-51.42	-50.66
4	-41.56	-56.05	-54.49
5	-54.47	-51.09	-23.56
6	29.41	63.93	34.52
7	30.98	62.21	31.22
8	28.35	62.55	34.21
9	-16.86	-15.33	-1.53
10	-43.46	-60.05	-46.58
11	-15.64	-13.26	-2.38
12	-8.54	-13.59	-5.05
13	-26.24	-66.56	-40.32
14	-6.19	-5.93	-0.25
Mean	-14.32	-15.09	-11.15

4.2 Fast Fourier Transform

A direct proof of the presence of a leading kinematic variable comes from the FFT of the measured θ. Fig.4 shows the FFT of the measured θ for each of the 14 tests. The plots in the logarithmic scale of the y-axis display the presence of a dominant peak in the range 0.3-1 Hz. The observation of the FFT plots reveals a dominant degree of freedom in a pretty wide range. The mechanical system is not elastic and exhibits a significant non-stationary or, possibly,

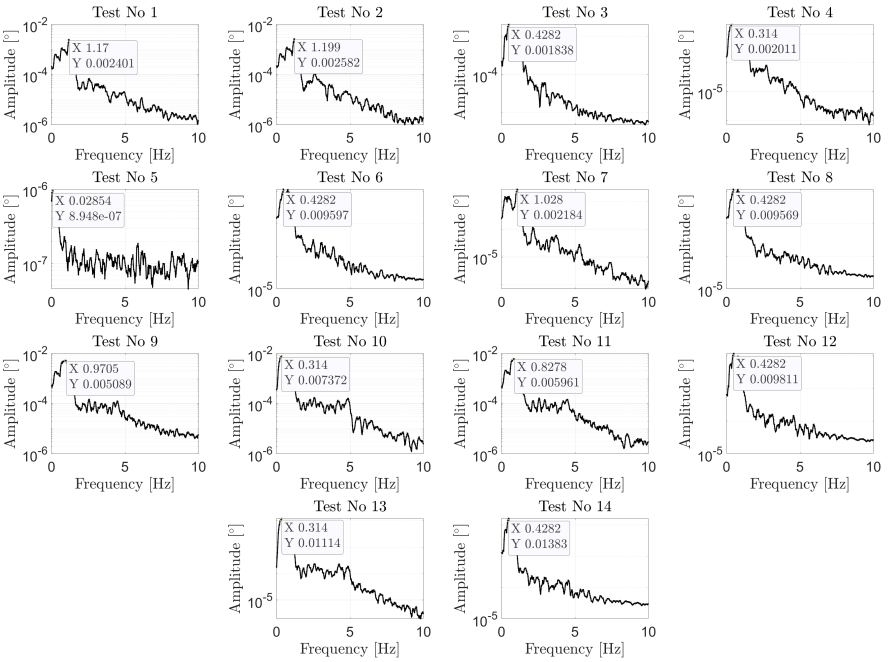

Fig. 4 Single side Fourier Spectrum of the base rotation (θ).

nonlinear response due to amplitude-dependent, hysteretic and degradation phenomena. The FFT helps prove the predominance of a single degree of freedom, but it does not provide information about the time-dependency of the response.

4.3 Spectrogram

Accordingly, the authors estimated the spectrograms of the θ signals. Spectrograms are visual representations of the spectrum of frequencies of a signal as it varies with time. Fig.5 shows the spectrograms of the measured θ for each of the 14 tests using an Hamming window with a 20% overlap. The spectrograms, represented by contour plots in greyscale, exhibits a moving high-amplitude and sharp peak in white, characterized by a significantly varying response. The authors evidenced the moving peak by plotting the high-amplitude frequency ridge in red. The inspection of the spectrograms reveals two aspects: (i) the sharpness of the peak further confirms the presence of a dominant degree of freedom; (ii) The significant variation of the frequency ridge proves that the system is not elastic and the model in Eq.8 is not adequate. It must include the effect of dissipation and the time-variability of the structural parameters.

The spectrograms can also reveal the possible nature of the system nonlinearity, helpful in enhancing the elastic model in Eq.8. Fig.6(a) superposes the

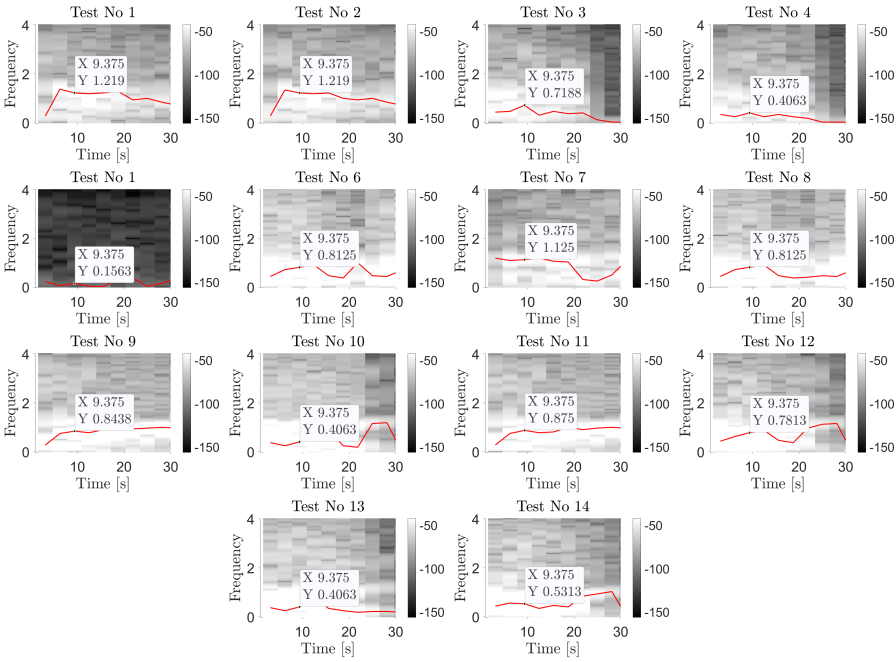

Fig. 5 Spectrogram of the base rotation (θ) with indication of the frequency ridge with highest amplitude. The X,Y in each subplot indicate the cartesian coordinates of the point the data tip refers to.

frequency ridges estimated in Fig.5 for each of the 14 tests. Fig.6(a) demonstrates the high variability of the peak response, but it does not provide information about the structural properties. Still, there is an evident reduction of the fundamental frequency from the 1st to the 14th test due to possible degradation phenomena (e.g, the shift of the pivot point due to the yielding of the base beam).

Fig.6(b) shows the frequency ridges as a function of the amplitude. The obtained plot is a rough estimation of the structural system's Frequency Response Function (FRF). The estimation of the FRF from seismic response data is an unconventional practice. Accurate FRF estimates should derive from sweep sine tests. However, despite the roughness of the estimation, the dots gather along two main branches, revealing a marked softening response. The fundamental frequency is amplitude-dependent, and the softening effect is related to nonlinear phenomena due to nonlinear terms in the governing equation. The stable and unstable curves of the FRF are quite evident, although the high-amplitude dots are limited. The softening frequency ridge showed in Fig.6(b) is qualitative and does not derive from a rigorous fitting. The experimental data are, in fact, inadequate for a proper characterization of a nonlinear softening system, since sweeping tests at different amplitude would be recommended for this purpose. A low number of points in correspondence of the high-amplitude response does not allow reliable estimation of the

nonlinear structural parameters from the fitting of the FRF. However, this qualitative outcome is used in the next section to enhance the mathematical model of the two-story building, inclusive of time-dependent parameters and nonlinear terms.

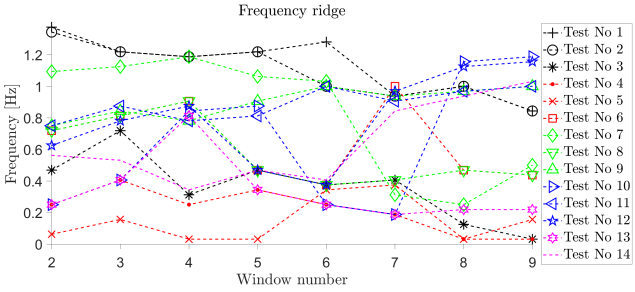

(a)

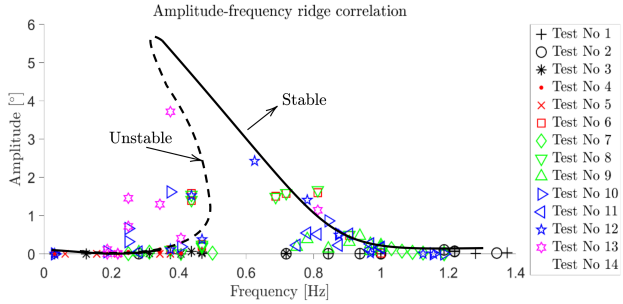

(b)

Fig. 6 (a) Frequency ridge as a function of the window number and test number; (b) Correlation between the frequency ridge and the response amplitude.

4.4 Hysteresis

Most dissipation in timber buildings depends on the hysteretic phenomena of steel connectors or dissipation devices. In the considered building, the pre-eminent dissipation source is the plasticization of the UFP connectors. Pei et al. [63] developed a flag-type hysteretic model representative of the nonlinear response of the tested building. The flag-type hysteretic model is characteristic of post-tensioned rocking structures. The hysteresis loop is very narrow compared to other hysteresis curves of timber-based systems due to the lack of pinching and manifest degradation phenomena.

The following considerations led the authors to model the rotational stiffness K_θ as elastic and reproduce the dissipation phenomena with an equivalent viscous term.

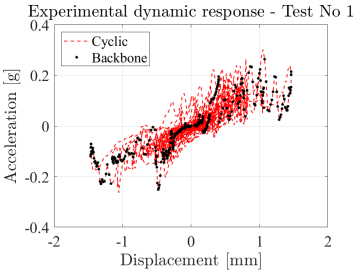

Fig. 7 Estimation of the backbone curve from the measured force-displacement curve of the first story in Test No 1. The resisting force is proportional to the inertial forces, therefore it is propositional to the measured acceleration, shown in the y-axis.

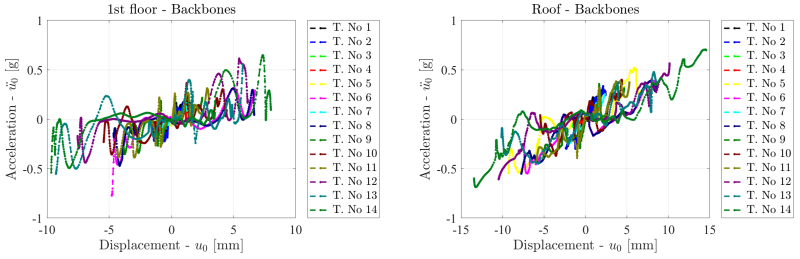

(a) (b)

Fig. 8 Superposition of the estimated backbone curves in terms of acceleration and floor displacement for all tests and the first (a) and second story (b).

- The hysteresis model developed by [59] has three phases. In the considered structural model, the total mass is lumped in the storeys. Consequently, the CLT panel does not possess any self-weight stabilizing moment, and the panel must rotate to achieve equilibrium with the external loads. Therefore, adopting the hysteretic model by [59], which distinguishes between the rocking and non-rocking phase, is inconsistent with the modelling choices in Fig.1.
- The narrowness and stability of the hysteresis loop may justify the modelling of dissipation with an equivalent viscous term. The shape of elliptic hysteresis curves, associated with viscosity, is not very dissimilar from flag-type hysteresis. Therefore, a displacement or energy equivalence can drive the assessment of an equivalent viscous term representative of a flag-type hysteresis curve. Besides, the direct displacement-based design procedure (DDBD) uses equivalent viscous damping and secant stiffness as proxies for the estimation of the nonlinear behaviour of structures. However, the available hysteretic models of timber structures are very elaborate, and the inelastic time-domain simulations using hysteretic models are not easily manageable. Hence, the adoption of equivalent viscous damping (EVD) is a crucial feature of any DDBD method.

- The hysteresis curves obtained from the experimental data by plotting the floor acceleration (proportional to the inertial forces) vs the storey displacement are very erratic and do not resemble the shape of any specific hysteresis curve. Fig.7 shows the estimated backbone of a sample data set, obtained by selecting the measurement points. The backbone curve is not linear and exhibits two phases, a first with lower stiffness, a second very irregular. Furthermore, the backbones of all the 14 tests in Fig.8 confirm that the hysteretic response of the structural system is very unpredictable and do not resemble the backbone of any specific hysteresis model. Therefore, the high uncertainty associated with estimating the hysteretic parameters supported a more straightforward approach based on equivalent viscosity, which mirrors the global structural dissipation without focusing on the hysteretic response.

5 Identification of the structural parameters

The selected results presented in the previous section showed that the SDOF mathematical model in Eq.8 could be a reasonable compromise between computational efficiency and prediction accuracy. However, Eq.8 has no dissipative neither nonlinear terms. Therefore, the authors upgraded Eq.8 by including a viscous term representative of dissipation phenomena and nonlinear terms representative of the softening response.

$$\ddot{\theta} + 4\pi\xi(\theta,\epsilon)f(\theta,\epsilon)\dot{\theta} + 4\pi^2 f(\theta,\epsilon)^2\theta = -\gamma\ddot{u}_g \tag{13}$$

where ξ is the equivalent damping ratio, f the natural frequency, $\gamma = S_x/I_\theta$, ϵ the dissipated energy. The model has two sources of nonlinearity. In particular, the natural frequency and damping ratio depend on both the rotation amplitude and the dissipated energy. The former aims at reproducing the softening behaviour of the rocking structure. The latter mirrors the effect of stiffness reduction observed between the 14 tests. As proven in the previous section, the natural frequencies globally reduce from the 1st to the 14th tests. The parameter γ can be estimated directly from the following equation:

$$\gamma = \frac{h_1 + k\,h_2}{h_1^2 + k\,h_2^2} \approx 0.18 \tag{14}$$

where $k = \frac{m_1}{m_2} = 1$ [63], $h_1 = 3.66$m and $h_2 = 6.71$m. Therefore, the unknown parameters are f and ξ. Eqs.15,16 express the possible nonlinear dependence of the natural frequency and damping ratio using a first-order approximation:

$$f = \hat{f}_0 + k_{f0,\epsilon}\epsilon - \left|\hat{k}_f + k_{kf,\epsilon}\epsilon\right|\theta \tag{15}$$

$$\xi = \hat{\xi}_0 + k_{\xi,\epsilon}\epsilon + \left|\hat{k}_\xi + k_{k\xi,\epsilon}\epsilon\right|\theta \tag{16}$$

where $\hat{f}_0$, $k_{f0,\epsilon}$, $\hat{k}_f$, $k_{kf,\epsilon}$, $\hat{\xi}_0$, $k_{\xi,\epsilon}$, $\hat{k}_\xi$, and $k_{k\xi,\epsilon}$ are correlation parameters. The effects of stiffness reduction are not very evident from a single test, but they manifest by comparing the 14 tests. Therefore, the authors estimated the parameters in Eqs.15-16 in a two-step procedure. In a first step, they estimated the amplitude nonlinearity by assuming the sole dependence on θ, as shown in Eqs.17-18.

$$f = f_0 - |k_f|\theta \tag{17}$$

$$\xi = \xi_0 + |k_\xi|\theta \tag{18}$$

Then they correlated f_0, k_f, ξ_0 and k_ξ to the dissipated energy, obtaining the parameters in Eqs.19-22.

$$f_0 = \hat{f}_0 + k_{f0,\epsilon}\epsilon \tag{19}$$

$$k_f = \hat{k}_f + k_{kf,\epsilon}\epsilon \tag{20}$$

$$\xi_0 = \hat{\xi}_0 + k_{\xi,\epsilon}\epsilon \tag{21}$$

$$k_\xi = \hat{k}_\xi + k_{k\xi,\epsilon}\epsilon \tag{22}$$

Eqs.17,18 modify Eq.13 into the following:

$$\ddot{\theta} + 4\pi(\xi_0 + |k_\xi|\theta)(f_0 - |k_f|\theta)\dot{\theta} + 4\pi^2(f_0 - |k_f|\theta)^2\theta = -\gamma\ddot{u}_g \tag{23}$$

where ξ_0, $|k_\xi|$, f_0, and $|k_f|$ are the unknown parameters.

5.1 First step of system identification

The authors estimated the unknown parameters by maximizing the rank correlation [70] between the solution of Eq.(13) and the experimental measurement:

$$\mathrm{corr}(\boldsymbol{\theta}_s, \boldsymbol{\theta}_e) = \frac{\boldsymbol{\theta}_s \cdot \boldsymbol{\theta}_e}{|\boldsymbol{\theta}_s| \cdot |\boldsymbol{\theta}_e|} \tag{24}$$

where $(\cdot)$ is the inner product, $|\,|$ the norm operator, $\boldsymbol{\theta}_e$ and $\boldsymbol{\theta}_s$ the experimental and simulated responses, respectively [71].

Tab.5 lists the estimated parameters of Eq.13, while Fig.9 shows the superposition between the experimental and simulated time histories of the base rotation (θ) for each of the 14 shake table tests. There is an optimum agreement between the experimental and simulated values of θ. The root mean square error between the two time-histories is minimal and validates the chosen mechanical model in Fig.1.
Still, the estimated parameters are not stationary and exhibit a variability between the 14 tests due to degradation phenomena. The estimation of the model degradation is crucial because it allows quantifying the structural resilience under repeated earthquakes.

The identified parameters in Tab.5 can lead to estimating the mechanical parameters of the governing equation. The concurrent estimation of the

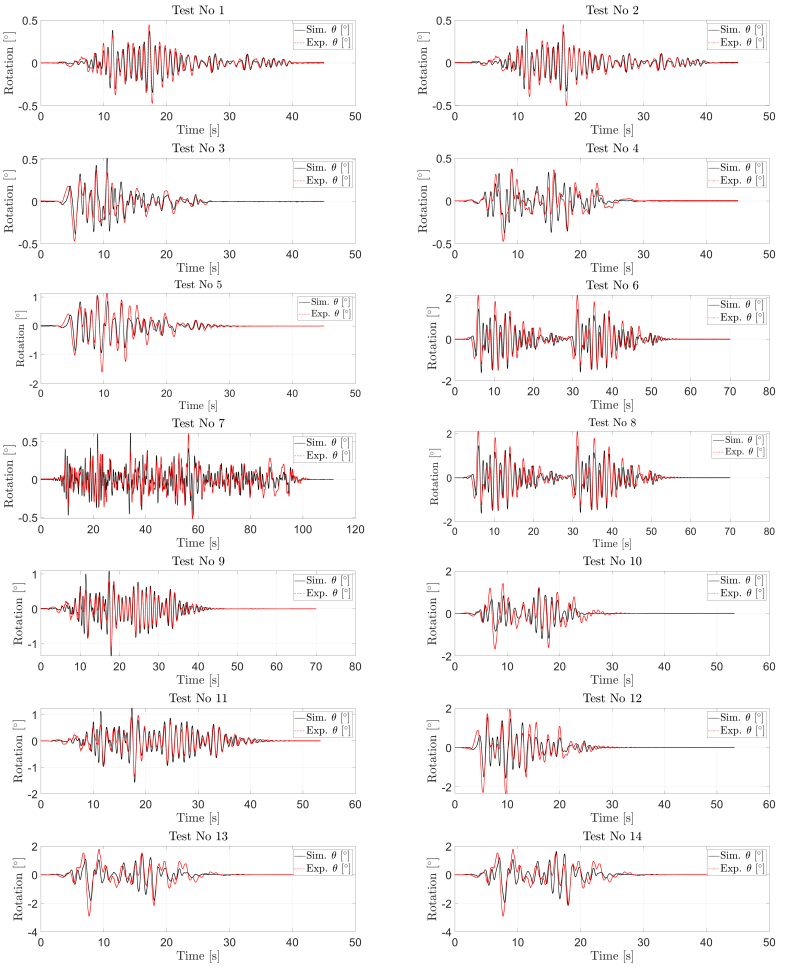

Fig. 9 Comparison between the experimental and simulated response in terms of base rotation θ.

Table 2 Root Mean Square Error between the experimental and simulated response in terms of base rotation θ, and estimated parameters of the analytical model.

Test No	RMSE	f_0 [Hz]	k_f [Hz]	ξ [%]	k_ξ [%]	γ
1	0.0098	1.2	62	12	89	0.18
2	0.0163	1.2	65	15	123	0.18
3	0.0159	1.5	89	35	116	0.18
4	0.0159	1.5	91	40	165	0.18
5	0.0492	1.0	123	23	184	0.18
6	0.1156	0.9	122	18	86	0.18
7	0.0355	1.2	104	46	196	0.18
8	0.1031	0.9	115	24	108	0.18
9	0.0531	1.0	105	21	97	0.18
10	0.0574	0.9	54	18	98	0.18
11	0.0578	1.0	55	18	92	0.18
12	0.0763	0.9	20	24	43	0.18
13	0.0786	0.8	85	34	56	0.18
14	0.074	0.8	86	35	57	0.18
Mean	0.0542	1.1	84	26	108	0.18

stiffness and inertial parameters is an undetermined problem. Therefore, the authors provide a reasonable approximation of the rotational stiffness ($\tilde{K}_\theta$) and estimate the rotational inertia ($\tilde{I}_\theta$). The rotational stiffness summates three contributions, the UFP dissipators, the pre-stressed tendons and the mass timber frame. Since the most significant contribution to the lateral stiffness is the rocking wall, and the frame's stiffness is challenging to estimate, the authors approximate the rotational stiffness by summating the sole tendons(K_{bars}) and UFP (K_{UFP}) contributions.

$$\tilde{K}_\theta = K_{UFP} + K_{bars} \approx n_s k_s b^2 + \sum_{i=1}^{n} \left(N_0 + E_s A_i \frac{b_i}{h} \right) b_i \tag{25}$$

where k_s is known from experimental tests on the UFP dissipators, see Tab.3. The approximate rotational inertia ($\tilde{I}_\theta$) is:

$$\tilde{I}_\theta = \frac{\tilde{K}_\theta}{(2\pi f_0)^2} \tag{26}$$

Assuming the identity of the story masses, the mass of each story is:

$$m_1 = m_2 = m = \frac{\tilde{I}_\theta}{h_1^2 + h_2^2} \tag{27}$$

Table 3 Estimate of the mechanical parameters in Eq.13.

$(2\pi f_0)^2$	γ	A_s	h	E_s	n	K_{bars}	k_s	n_s	K_{UFP}	$\tilde{K}_\theta$	$\tilde{I}_\theta$
[Hz^2]	[m^{-1}]	[mm^2]	[m]	[GPa]		[kNm]	[kN/mm]	/	[kNm]	[kNm]	[t·m^2]
44.07	0.18	215.5	7.32	210	16	8120	6.5	10	153155	161274	3660

Tab.3 reports the estimated mechanical parameters and the values of those assumed for their estimation following Eq.26-27.

5.2 Second step of system identification

The variation of the modelling parameters between the 14 tests depends on minor degradation phenomena compared to traditional mass timber structures. Although these phenomena are trivial in a single seismic simulation, their effect can be more consistent under repeated earthquakes. Therefore, following a conventional approach in structural engineering, the authors correlated the parameters in Tab.5 to the cumulative dissipated energy between the 14 tests.

Fig.10 plots the dissipated energy in the 14 tests as a function of time. The cumulation of the maximum values of the dissipated energy is used to derive the correlation parameters of the four variables f_0, k_f, ξ and k_ξ using

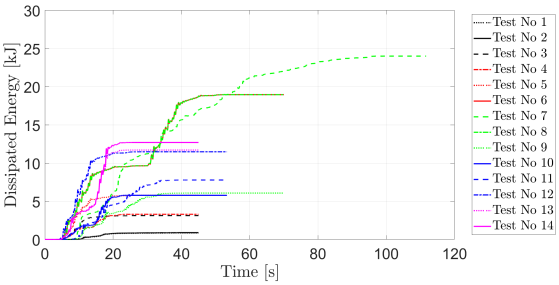

Fig. 10 Dissipated energy of the SDOF in each of the 14 tests.

an Ordinary Least Squares (OLS) optimization:

$$f_0 = \hat{f}_0 + k_{f0,\epsilon}\epsilon \tag{28}$$

$$k_f = \hat{k}_f + k_{kf,\epsilon}\epsilon \tag{29}$$

$$\xi = \hat{\xi}_0 + k_{\xi,\epsilon}\epsilon \tag{30}$$

$$k_\xi = \hat{k}_\xi + k_{k\xi,\epsilon}\epsilon \tag{31}$$

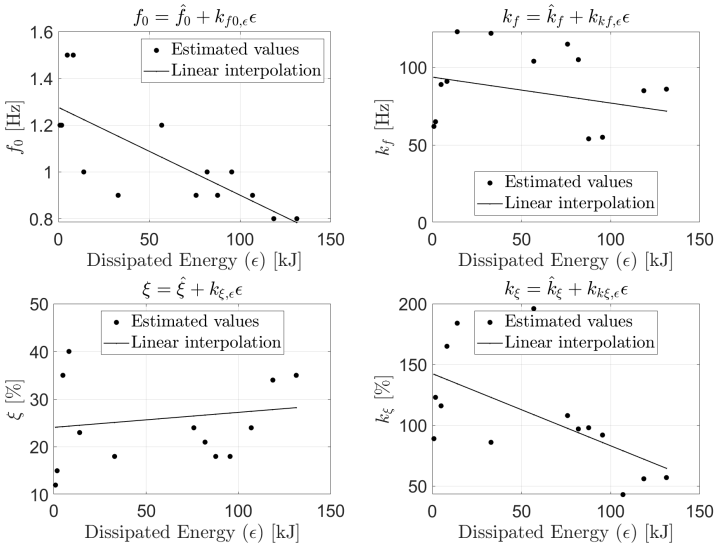

Fig. 11 Correlation between the estimated model parameters and the cumulative maximum dissipated energy.

Fig.11 shows that the nonlinear effects related to the k_f coefficient are not markedly dependent on the cumulative dissipated energy. Conversely, the natural frequency f_0 and the nonlinear damping term k_ξ exhibit evident negative correlations. The results demonstrate that damage accumulation causes

a global stiffness reduction, mainly due to the shift of the pivot point and a reduction of the dissipation capacity at higher displacement values.

Table 4 Estimated values of Eqs.28-31, see Fig.11. The first row shows the parameters obtained from the calibration with all data. The remaining rows from the first to the fourteenth correspond to the calibration based on the leave-one-out cross-validation approach, i.e. calibrating by progressively removing one data point from the data set for a cross-validation.

Label	$\hat{f}_0$ [Hz]	$k^a_{f0,\epsilon}$	$\hat{k}_f$	$k^b_{kf,\epsilon}$	$\hat{\xi}_0$ [%]	$k^c_{\xi,\epsilon}$	$\hat{k}_\xi$	$k^b_{k\xi,\epsilon}$
All	1.276237	-0.00375	93.7436	-0.16698	24.09526	0.031418	142.4543	-0.59289
1	1.29	-0.0039	101.02	-0.24	26.89	0.0018	154.64	-0.72
2	1.29	-0.0039	100.20	-0.24	26.17	0.0095	146.64	-0.64
3	1.22	-0.0032	94.59	-0.18	21.77	0.0554	147.55	-0.65
4	1.22	-0.0032	94.03	-0.17	20.88	0.0637	136.83	-0.54
5	1.32	-0.0042	87.83	-0.11	24.38	0.0287	133.13	-0.50
6	1.31	-0.0040	89.17	-0.13	25.06	0.0245	147.46	-0.63
7	1.27	-0.0037	92.16	-0.17	22.48	0.0325	135.46	-0.59
8	1.28	-0.0037	92.41	-0.19	24.19	0.0330	142.04	-0.60
9	1.28	-0.0038	93.09	-0.19	24.24	0.0365	142.37	-0.60
10	1.28	-0.0037	94.09	-0.14	24.22	0.0414	142.35	-0.60
11	1.28	-0.0039	93.66	-0.13	24.06	0.0447	142.48	-0.60
12	1.28	-0.0038	91.99	-0.06	23.99	0.0383	141.32	-0.52
13	1.27	-0.0037	94.43	-0.20	24.48	0.0154	141.45	-0.55
14	1.28	-0.0038	95.19	-0.22	24.79	0.0085	141.68	-0.57

a) [Hz·kJ^{-1}]; b) [kJ^{-1}]; c) [% ·kJ^{-1}]

Tab.4 lists the estimated parameters of Eqs.28-31 plotted in Fig.11.

Table 5 Root Mean Square Error between the experimental and simulated response in terms of base rotation θ, and estimated parameters of the analytical model.

Test No	RMSE	f_0 [Hz]	k_f [Hz]	ξ [%]	k_ξ [%]	γ
1	0.0098	1.2	62	12	89	0.18
2	0.0163	1.2	65	15	123	0.18
3	0.0159	1.5	89	35	116	0.18
4	0.0159	1.5	91	40	165	0.18
5	0.0492	1.0	123	23	184	0.18
6	0.1156	0.9	122	18	86	0.18
7	0.0355	1.2	104	46	196	0.18
8	0.1031	0.9	115	24	108	0.18
9	0.0531	1.0	105	21	97	0.18
10	0.0574	0.9	54	18	98	0.18
11	0.0578	1.0	55	18	92	0.18
12	0.0763	0.9	20	24	43	0.18
13	0.0786	0.8	85	34	56	0.18
14	0.074	0.8	86	35	57	0.18
Mean	0.0542	1.1	84	26	108	0.18

The model calibration with all data might conceal over-fitting issues without a proper validation procedure, which usually requires distinguishing between a training set and a test set. However, it is challenging to prove the absence of overfitting issues with a few data, just 14 in this case. Therefore, the authors, following [72], adopted the leave-one-out cross-validation (LOOCV) approach. The model has been recalibrated by progressively removing one data point while using the remaining for calibration, and the removed data point for validation. This procedure is repeated 14 times for each data point.

If the error metrics do not present substantial changes between models, it is unlikely to have overfitting issues. Tab.4 shows the estimated parameters for each calibration step, from the first with all data to the fourteenth based on the leave-one-out cross-validation procedure. Fig.12 compares the model predictions with the experimental values in terms of maximum rotation. Interestingly, the error metrics do not change between each model, yielding an $R^2 \approx 0.8$. Therefore, the proposed model does not appear to suffer from overfitting issues.

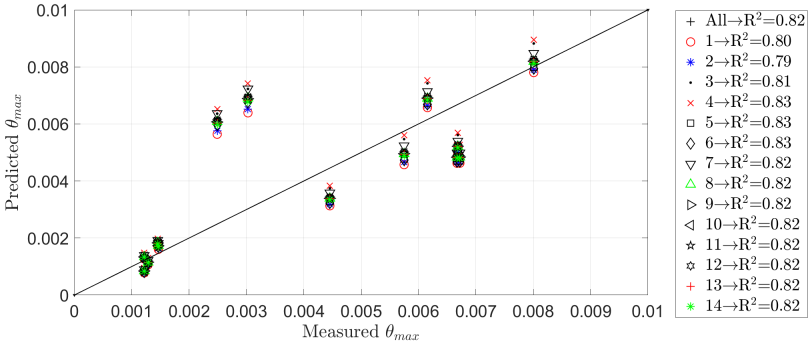

Fig. 12 Leave-one-out cross-validation calibration to prove the absence of over fitting issues. The quality of the fitting is shown by plotting the maximum measured and estimated base rotations. The first calibration (All) is obtained with all data, while the following by progressively removing one earthquake simulation from the dataset, labelled from 1 to 14.

5.3 Discussion on the parameters variability

The averaged parameters estimated in the first four tests refer to the SLE condition, characterized by a lower PGA level up to 0.2g. The averaged parameters in Tab.6 are used to predict the response under different excitation levels characterized by PGA in the range 0.2-1-2g. The analysis assesses if there is a specif level for the calibration of the parameters minimizing the error of the estimates. Tab.7 lists the error related to the estimate of the displacement in

Table 6 Avaraged parameters estimated between in Tests No 1-4 referred to the SLE

f_0	k_f	ξ	k_ξ	γ
1.4	83.9	32.8	144.1	0.2

the 14 tests in terms of Root Mean Square Error (RMSE), Maximum error (ME) and Relative Maximum Error (RME) between the experimental (θ_e) and simulated (θ_s) base rotations. As expected, predicting the displacement response in the first four tests is entirely accurate, leading to an average error of 1%. The same parameters yield a higher error, 20% on average, in the tests characterized by higher PGA. Still, the prediction can be considered reasonably accurate for engineering purposes, despite the variability related to the

Table 7 Root Mean Square Error (RMSE), Maximum error (ME) and Relative Maximum Error (RME) between the experimental (θ_e) and simulated (θ_s) response in terms of base rotation.

Test No	RMSE(θ_e-θ_s) []	Max(θ_e-θ_s) []	Max(θ_e-θ_s)/Max(θ_e) [%]
1	0.0450	0.0191	22.73%
2	0.0484	0.0252	30.27%
3	0.0339	-0.0257	-36.77%
4	0.0327	-0.0155	-22.14%
Avarage	0.0400	0.0008	-1.48%

Test No	RMSE(θ_e-θ_s) []	Max(θ_e-θ_s) []	Max(θ_e-θ_s)/Max(θ_e) [%]
5	0.1940	-0.1086	-28.35%
6	0.2334	0.2717	70.51%
7	0.0478	-0.0198	-26.92%
8	0.2339	0.2476	64.74%
9	0.1862	0.0042	2.92%
10	0.1537	0.2166	84.84%
11	0.2130	0.1349	77.78%
12	0.2357	-0.2205	-62.48%
13	0.2373	0.4875	147.97%
14	0.2976	-0.4838	-105.38%
Avarage	0.2033	0.0530	22.56%

model approximation.

The use of the parameters in Tab.6 leads, on average, to an underestimation of the structural response at higher displacement levels. This effect mostly depends on the correct choice of the natural frequency related to minor degradation phenomena (reducing the pivot length due to local plasticization, e.g.). However, a close inspection of Tab.7 reveals that the error is both positive and negative even at higher displacement levels. Therefore, the error cannot be removed by simply reducing the natural frequency or adopting other intensity levels to calibrate the parameters. On the other hand, the SLE excitation yields satisfactory results at higher PGAs, proving that the structural system exhibits a mostly linear response related to minor degradation phenomena.

6 Estimate of the limit state of the post-tensioned tendons

The assessment of the fragility functions of the considered structural model with degradation entails the evaluation of the base rotation associated with a given limit state. The authors assume that the limit state of the structure corresponds to the limit state of the post-tensioned tendons. The axial deformation of the i-th steel bar, ϵ_s^i, can be written as a function of the base rotation θ:

$$\epsilon_s^i = \sqrt{\theta^2 + \left(1 + \theta \frac{b_i}{h}\right)^2} - 1 \tag{32}$$

The limit state rotation of the i-th bar $\theta_{f,i}$ can be derived from the inversion of Eq.32 by setting ϵ_s^i equal to the yielding deformation of steel, $\epsilon_{s,y}$. Eq.32 is

a 2nd order algebraic equation with the following two solutions:

$$\theta_f = \left\{ -\frac{h\left(h\sqrt{\frac{b_i^2(\epsilon_{s,y}+1)^2+h^2\epsilon_{s,y}(\epsilon_{s,y}+2)}{h^2}}+b_i\right)}{b_i^2+h^2}, +\frac{h\left(h\sqrt{\frac{b_i^2(\epsilon_{s,y}+1)^2+h^2\epsilon_{s,y}(\epsilon_{s,y}+2)}{h^2}}-b_i\right)}{b_i^2+h^2} \right\} \tag{33}$$

Eq.32 is obtained by assuming as positive the clockwise direction of the rocking panel. Therefore, the solution with physical meaning is the positive one:

$$\theta_f = \frac{h\left(h\sqrt{\frac{b_i^2(\epsilon_{s,y}+1)^2+h^2\epsilon_{s,y}(\epsilon_{s,y}+2)}{h^2}}-b_i\right)}{b_i^2+h^2} \tag{34}$$

By assuming a conservative collapse condition corresponding to the bar yielding, the assumed limit steel deformation, $\epsilon_{s,y}$, is equal to 0.0021%. The angle associated with the limit state of the post-tensioned bar is:

$$\theta_{f,\text{bar}} = 0.95^\circ \tag{35}$$

The failure angle in Eq.35 is the minimum between the values obtained with the two b_i, equal to the distance between the pivot point and the bar direction, see Tab.8

Table 8 Estimated values of the yielding and ultimate base rotation of the CLT panel; b_1 and b_2 are the two distances between the bar and the pivot point, h the panel's height, ϵ_y and ϵ_u yielding and ultimate steel deformation, θ_y^1 and θ_u^1 yielding and ultimate base rotations corresponding to b_1, θ_y^2 and θ_u^2 yielding and ultimate base rotations corresponding to b_2.

b_1 [m]	b_2 [m]	h [m]	ϵ_y [%]	ϵ_u [%]	θ_y^1 []	θ_f^1 []	θ_y^2 []	θ_f^2 []
0.89	0.64	7.32	0.0021	0.08	0.95	16.60	1.24	18.80

7 Fragility functions under repeated earthquakes

The authors estimated the fragility functions of the tested structure under repeated earthquakes from truncated incremental dynamic analysis (TIDA) using the model with parameters in tab.4. In post-tensioned or self-centring structures, both the residual and the maximum rotation represent significant control parameters. However, in this paper, the authors will use the sole maximum rotation due to the intrinsic limitations of the proposed elastic model, which cannot predict residual rotation values. The exceeding of the θ value in Eq.35 identifies the failure domain.

The fragility functions do not express the collapse probability, but the probability of exceeding a specific limit state, associated with the yielding of the

post-tensioning bars, as formulated in Eq.33. Therefore, the assumption of the considered limit state is in line with the modelling choices, which do not include structural nonlinearities due to failures of the structural components. Besides, the assumption of this limit state does not require a model extrapolation because the tested building experienced the post-tensioning bar yielding during the shake table tests used for the model validation. Following the approach in [14, 73], the list of 41 Italian earthquake records with magnitude ranging between 5 and 6.5, given in Tab. 9, represented the base for generating 41 artificial earthquakes, scaled to the same Peak Ground Acceleration (PGA) and optimized to match the design spectrum. Each earthquake is concatenated three times, resulting in a sequence of three identical seismic events. The earthquake records are homogenized to the same intensity level and optimized to match the design spectrum expected in L'Aquila (Italy) according to the national seismic code using the algorithm by [74]. A lognormal cumulative distribution function fits the fragility function from data collected from nonlinear dynamic analyses [75]:

$$P(C|IM = x) = \Phi\left(\frac{ln(x/\theta)}{\beta}\right) \tag{36}$$

where $P(C|IM = x)$ is the probability that a ground motion with $IM = x$ will cause the structure to exceed the considered limit state; Φ is the standard normal cumulative distribution function (CDF); θ is the median of the fragility function (the IM level with 50% probability of exceeding the considered limit state); and β is the standard deviation of ln IM. The TIDA leads to an alternative procedure [75] to estimate the parameters θ and β, obtained by varying the parameters until maximizing a specific likelihood function. Specifically, the parameters are obtained by maximizing the logarithm of the following likelihood function:

$$\{\hat{\theta}, \hat{\beta}\} = \arg\max_{\hat{\theta},\hat{\beta}} \sum_{j=1}^{m} \left[\ln \Phi\left(\frac{\ln(IM_i/\theta)}{\beta}\right)\right] + [n-m] ln \left[1 - \Phi\left(\frac{\ln(IM_{max}/\theta)}{\beta}\right)\right] \tag{37}$$

where $\hat{}$ denotes an estimated parameter, $\Phi()$ the standard normal distribution PDF, n the number of ground motion used in the analysis, m the number of m ground motions that caused the limit state exceeding at IM levels lower than IM_{max}, $\Phi()$ the standard normal distribution CDF. The authors estimated the parameters of Eq.(37) for each of the 41 earthquake records. The resulting two parameters of the fragility function, representative of all considered seismic scenarios, are obtained taking the mean of all the couples of parameters estimated from each TIDA.

Fig.13 shows the response of the structure under the repetition of earthquake No 1 (see Tab.9). The effect of damage accumulation produces an increment of the maximum θ value attained during the structural response.

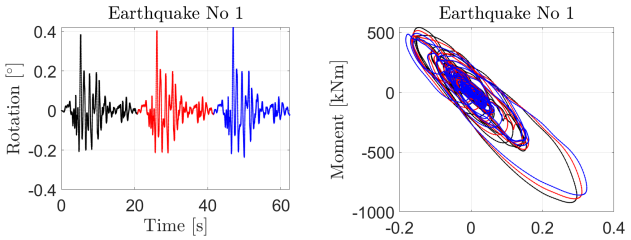

(a) (b)

Fig. 13 Response of the considered SDOF oscillator with.

The plot of the maximum θs in Fig.14(a) as a function of the spectral acceleration (Sa) demonstrates the effect of stiffness reduction between the three earthquake repetitions, identified by three different colours: black the first repetition, red the second repetition and blue the third repetition. If successive earthquakes occur, the structure reaches the limit state associated with the bar yielding with a lower Sa.

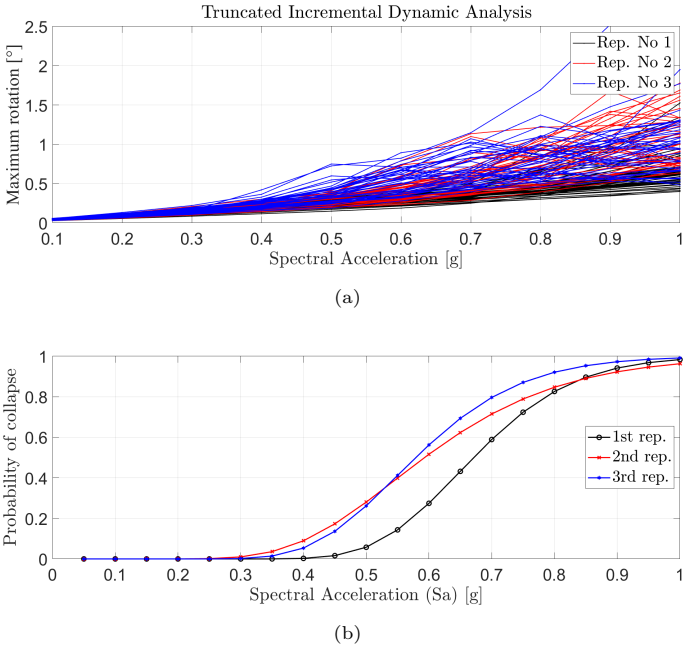

(a)

(b)

Fig. 14 Results of the Truncated Incremental Dynamic Analyses (a) and fragility curves (b) using three concatenations of each of the 41 earthquakes in Tab.9, Rep. stands for the number of earthquake repetition.

The effect of damage accumulation is evident from the estimated fragility functions, plotted in Fig.14(b). Earthquake repetitions determine a shift of the fragility function in the left direction, displaying a more fragile performance.

8 Conclusions

This paper investigates the seismic response of a resilient two-storeys mass timber building from shaking table tests. The authors enhanced the mechanical model proposed by [63], which was used to derive the fragility curves of the considered building under repeated earthquakes. The primary outcomes of this research are:

- The presence of a rocking post-tensioned Cross-Laminated Timber (CLT) panel, free to uplift, and connected to each storey, determines the substantive reduction of the building degrees of freedom to the sole base rotation. Under reasonable kinematic assumptions based on the geometrical and constructive features of the building, the authors derived the governing equation of the structural response.
- The model's hypotheses are validated through selected experimental results, which proved that the base rotation is the prevalent degree of freedom and that the CLT wall behaves substantially like a rigid block.
- The experimental data of the 14 shake table tests led to the estimation of the parameters of the governing equation, corrected by first-order approximations to include nonlinear and degradation effects. Furthermore, the simulated and experimental responses in terms of base rotation show a satisfactory agreement.
- The model is used to estimate the fragility functions of the building under three repeated earthquakes. The structural response is very stable after repeated earthquakes, compared to traditional mass timber buildings, which manifest a dramatic reduction of their initial capacity.

9 Data Availability Statement

All data, models, or code that support the findings of this study are available from the corresponding author upon reasonable request.

References

[1] Johnston, H., Watson, C., Pampanin, S., Palermo, A.: Shake table testing of an integrated low damage building system. In: 2nd European Conference in Earthquake Engineering and Seismology, Istanbul, pp. 25–29 (2014)

[2] van de Lindt, J.W., Bahmani, P., Mochizuki, G., Pryor, S.E., Gershfeld, M., Tian, J., Symans, M.D., Rammer, D.: Experimental seismic behavior of a full-scale four-story soft-story wood-frame building with retrofits.

ii: shake table test results. Journal of Structural Engineering **142**(4), 4014004 (2016)

[3] Van de Lindt, J.W., Pei, S., Pryor, S.E., Shimizu, H., Isoda, H.: Experimental seismic response of a full-scale six-story light-frame wood building. Journal of Structural Engineering **136**(10), 1262–1272 (2010)

[4] Gavric, I., Fragiacomo, M., Ceccotti, A.: Cyclic behaviour of typical metal connectors for cross-laminated (clt) structures. Materials and structures **48**(6), 1841–1857 (2015)

[5] Zhang, X., Isoda, H., Sumida, K., Araki, Y., Nakashima, S., Nakagawa, T., Akiyama, N.: Seismic performance of three-story cross-laminated timber structures in japan. Journal of Structural Engineering **147**(2), 04020319 (2021)

[6] Faggiano, B., Iovane, G., Tartaglia, R., Ciccone, G., Landolfo, R., Mazzolani, F.M., Andreolli, M., Tomasi, R., Piazza, M.: Numerical simulation of monotonic tests on beam-column timber joints equipped with steel links for heavy timber seismic resistant mrf. In: AIP Conference Proceedings, vol. 2116, p. 260017 (2019). AIP Publishing LLC

[7] Aloisio, A., Boggian, F., Tomasi, R., Fragiacomo, M.: The role of the hold-down in the capacity model of ltf and clt shear walls based on the experimental lateral response. Construction and Building Materials **289**, 123046 (2021)

[8] Sandoli, A., DAmbra, C., Ceraldi, C., Calderoni, B., Prota, A.: Sustainable cross-laminated timber structures in a seismic area: Overview and future trends. Applied Sciences **11**(5), 2078 (2021)

[9] Izzi, M., Casagrande, D., Bezzi, S., Pasca, D., Follesa, M., Tomasi, R.: Seismic behaviour of cross-laminated timber structures: A state-of-the-art review. Engineering Structures **170**, 42–52 (2018)

[10] Brandner, R., Flatscher, G., Ringhofer, A., Schickhofer, G., Thiel, A.: Cross laminated timber (clt): overview and development. European Journal of Wood and Wood Products **74**(3), 331–351 (2016)

[11] Hristovski, V., Dujic, B., Stojmanovska, M., Mircevska, V.: Full-scale shaking-table tests of xlam panel systems and numerical verification: Specimen 1. Journal of Structural Engineering **139**(11), 2010–2018 (2013)

[12] Ceccotti, A., Sandhaas, C., Okabe, M., Yasumura, M., Minowa, C., Kawai, N.: Sofie project–3d shaking table test on a seven-storey full-scale cross-laminated timber building. Earthquake Engineering & Structural Dynamics **42**(13), 2003–2021 (2013)

[13] van de Lindt, J.W., Furley, J., Amini, M.O., Pei, S., Tamagnone, G., Barbosa, A.R., Rammer, D., Line, P., Fragiacomo, M., Popovski, M.: Experimental seismic behavior of a two-story clt platform building. Engineering Structures **183**, 408–422 (2019)

[14] Aloisio, A., Alaggio, R., Fragiacomo, M.: Equivalent viscous damping of cross-laminated timber structural archetypes. Journal of Structural Engineering **147**(4), 04021012 (2021)

[15] Pei, S., Van De Lindt, J., Popovski, M., Berman, J., Dolan, J., Ricles, J., Sause, R., Blomgren, H., Rammer, D.: Cross-laminated timber for seismic regions: Progress and challenges for research and implementation. Journal of Structural Engineering **142**(4), 2514001 (2016)

[16] Aloisio, A., Alaggio, R., Köhler, J., Fragiacomo, M.: Extension of generalized bouc-wen hysteresis modeling of wood joints and structural systems. Journal of Engineering Mechanics **146**(3), 04020001 (2020)

[17] Marano, G.C., Pelliciari, M., Cuoghi, T., Briseghella, B., Lavorato, D., Tarantino, A.M.: Degrading bouc-wen model parameters identification under cyclic load. International Journal of Geotechnical Earthquake Engineering **8**(2), 60–81 (2017). https://doi.org/10.4018/IJGEE.2017070104

[18] Greco, R., Monti, G., Marano, G.C.: Influence of post-yield stiffness on inelastic seismic response: A stochastic analysis. International Journal of Structural Stability and Dynamics **17**(2) (2017). https://doi.org/10.1142/S0219455417500286

[19] Jorissen, A., Fragiacomo, M.: General notes on ductility in timber structures. Engineering structures **33**(11), 2987–2997 (2011)

[20] Chen, J., Chen, Y.F., Shi, X., Zhao, Y., Li, T.: Hysteresis behavior of traditional timber structures by full-scale tests. Advances in Structural Engineering **21**(2), 287–299 (2018)

[21] Pu, W., Liu, C., Dai, F.: Optimum hysteretic damper design for multistory timber structures represented by an improved pinching model. Bulletin of Earthquake Engineering **16**(12), 6221–6241 (2018)

[22] Di Gangi, G., Demartino, C., Quaranta, G., Monti, G.: Dissipation in sheathing-to-framing connections of light-frame timber shear walls under seismic loads. Engineering Structures **208**, 110246 (2020)

[23] Restrepo, J.I., Rahman, A.: Seismic performance of self-centering structural walls incorporating energy dissipators. Journal of Structural Engineering **133**(11), 1560–1570 (2007)

[24] Kode, A., Amini, M.O., van de Lindt, J.W., Line, P.: Lateral load testing of a full-scale cross-laminated timber diaphragm. Practice Periodical on Structural Design and Construction **26**(2), 04021001 (2021)

[25] Aloisio, A., Boggian, F., Tomasi, R.: Design of a novel seismic retrofitting system for rc structures based on asymmetric friction connections and clt panels. Engineering Structures **254**, 113807 (2022)

[26] Kramer, A., Barbosa, A.R., Sinha, A.: Performance of steel energy dissipators connected to cross-laminated timber wall panels subjected to tension and cyclic loading. Journal of Structural Engineering **142**(4), 4015013 (2016)

[27] Hashemi, A., Zarnani, P., Quenneville, P.: Seismic assessment of rocking timber walls with energy dissipation devices. Engineering Structures **221**, 111053 (2020)

[28] Wakashima, Y., Ishikawa, K., Shimizu, H., Kitamori, A., Matsubara, D., Tesfamariam, S.: Dynamic and long-term performance of wood friction connectors for timber shear walls. Engineering Structures **241**, 112351 (2021)

[29] Aloisio, A., Contento, A., Alaggio, R., Briseghella, B., Fragiacomo, M.: Probabilistic assessment of a light-timber frame shear wall with variable pinching under repeated earthquakes. Journal of Structural Engineering **148**(11), 04022178 (2022)

[30] Aloisio, A., Pelliciari, M., Bergami, A.V., Alaggio, R., Briseghella, B., Fragiacomo, M.: Effect of pinching on structural resilience: performance of reinforced concrete and timber structures under repeated cycles. Structure and Infrastructure Engineering, 1–17 (2022)

[31] Loo, W.Y., Quenneville, P., Chouw, N.: A numerical study of the seismic behaviour of timber shear walls with slip-friction connectors. Engineering Structures **34**, 233–243 (2012)

[32] Chan, N., Hashemi, A., Zarnani, P., Quenneville, P.: Pinching-free connector for timber structures. Journal of Structural Engineering **147**(5), 04021036 (2021)

[33] Li, Z., Chen, F., He, M., Zhou, R., Cui, Y., Sun, Y., He, G.: Lateral performance of self-centering steel–timber hybrid shear walls with slip-friction dampers: Experimental investigation and numerical simulation. Journal of Structural Engineering **147**(1), 04020291 (2021)

[34] Wakashima, Y., Shimizu, H., Ishikawa, K., Fujisawa, Y., Tesfamariam, S.: Friction-based connectors for timber shear walls: static experimental

tests. Journal of Architectural Engineering **25**(2), 04019006 (2019)

[35] Dong, H., He, M., Christopoulos, C., Li, Z.: Quasi-static tests and parametric simulations of hybrid steel frame and light wood shear walls with frictional dampers. Engineering Structures **228**, 111485 (2021)

[36] Fitzgerald, D., Sinha, A., Miller, T.H., Nairn, J.A.: Axial slip-friction connections for cross-laminated timber. Engineering Structures **228**, 111478 (2021)

[37] Asgari, H., Tannert, T., Ebadi, M.M., Loss, C., Popovski, M.: Hyperelastic hold-down solution for clt shear walls. Construction and Building Materials **289**, 123173 (2021)

[38] Loo, W.Y., Kun, C., Quenneville, P., Chouw, N.: Experimental testing of a rocking timber shear wall with slip-friction connectors. Earthquake Engineering & Structural Dynamics **43**(11), 1621–1639 (2014)

[39] Loo, W.Y., Quenneville, P., Chouw, N.: Rocking timber structure with slip-friction connectors conceptualized as a plastically deformable hinge within a multistory shear wall. Journal of Structural Engineering **142**(4), 4015010 (2016)

[40] Tesfamariam, S., Wakashima, Y., Skandalos, K.: Damped timber shear wall: Shake-table tests and analytical models. Journal of Structural Engineering **147**(6), 04021064 (2021)

[41] Boggian, F., Tardo, C., Aloisio, A., Marino, E.M., Tomasi, R.: Experimental cyclic response of a novel friction connection for seismic retrofitting of rc buildings with clt panels. Journal of Structural Engineering **148**(5), 04022040 (2022)

[42] Pei, S., Van de Lindt, J., Barbosa, A.R., Berman, J., Blomgren, H.-E., Dolan, J., McDonnell, E., Zimmerman, R., Fragiacomo, M., Rammer, D.: Full-scale shake table test of a two story mass-timber building with resilient rocking walls. In: In: Proceedings, 16th European Conference on Earthquake Engineering. Thessaloniki, Greece: 1-10., pp. 1–10 (2018)

[43] Brown, J.R., Li, M., Palermo, A., Pampanin, S., Sarti, F.: Experimental testing of a low-damage post-tensioned c-shaped clt core-wall. Journal of Structural Engineering **147**(3), 04020357 (2021)

[44] Di Cesare, A., Ponzo, F.C., Nigro, D., Pampanin, S., Smith, T.: Shaking table testing of post-tensioned timber frame building with passive energy dissipation systems. Bulletin of Earthquake Engineering **15**(10), 4475–4498 (2017)

[45] Di Cesare, A., Ponzo, F.C., Lamarucciola, N., Nigro, D.: Experimental seismic response of a resilient 3-storey post-tensioned timber framed building with dissipative braces. Bulletin of Earthquake Engineering **18**(15), 6825–6848 (2020)

[46] Buchanan, A., Deam, B., Fragiacomo, M., Pampanin, S., Palermo, A.: Multi-storey prestressed timber buildings in new zealand. Structural Engineering International **18**(2), 166–173 (2008)

[47] Palermo, A., Pampanin, S., Fragiacomo, M., Buchanan, A., Deam, B.: Innovative seismic solutions for multi-storey lvl timber buildings (2006)

[48] Iqbal, A., Pampanin, S., Palermo, A., Buchanan, A.: Performance and design of lvl walls coupled with ufp dissipaters. Journal of Earthquake Engineering **19**(3), 383–409 (2015)

[49] Iqbal, A., Smith, T., Pampanin, S., Fragiacomo, M., Palermo, A., Buchanan, A.: Experimental performance and structural analysis of plywood-coupled lvl walls. Journal of Structural Engineering **142**(2), 04015123 (2016)

[50] Iqbal, A., Pampanin, S., Buchanan, A.H.: Seismic performance of full-scale post-tensioned timber beam-column connections. Journal of Earthquake Engineering **20**(3), 383–405 (2016)

[51] Chen, Z., Popovski, M., Iqbal, A.: Structural performance of post-tensioned clt shear walls with energy dissipators. Journal of Structural Engineering **146**(4), 04020035 (2020)

[52] Palermo, A., Sarti, F., Baird, A., Bonardi, D., Dekker, D., Chung, S.: From theory to practice: Design, analysis and construction of dissipative timber rocking post-tensioning wall system for carterton events centre, new zealand. In: Proceedings of the 15th World Conference on Earthquake Engineering, Lisbon, Portugal, pp. 24–28 (2012)

[53] Holden, T., Devereux, C., Haydon, S., Buchanan, A., Pampanin, S.: Innovative structural design of a three storey poststensioned timber building. World **15**, 19 (2012)

[54] Ganey, R., Berman, J., Akbas, T., Loftus, S., Daniel Dolan, J., Sause, R., Ricles, J., Pei, S., Lindt, J.v.d., Blomgren, H.-E.: Experimental investigation of self-centering cross-laminated timber walls. Journal of Structural Engineering **143**(10), 04017135 (2017)

[55] Akbas, T., Sause, R., Ricles, J.M., Ganey, R., Berman, J., Loftus, S., Dolan, J.D., Pei, S., van de Lindt, J.W., Blomgren, H.-E.: Analytical and experimental lateral-load response of self-centering posttensioned clt

walls. Journal of Structural Engineering **143**(6), 04017019 (2017)

[56] Baas, E.J., Riggio, M., Barbosa, A.R.: Structural health monitoring data collected during construction of a mass-timber building with a data platform for analysis. Data in Brief **35**, 106845 (2021)

[57] He, M., Zheng, X., Lam, F., Li, Z.: Potential loss in prestressing tendon forces under long-term service conditions: cross-laminated timber shear wall applications. Journal of Structural Engineering **148**(3), 04021284 (2022)

[58] Zheng, X., He, M., Li, Z., Luo, Q.: Long-term performance of post-tensioned cross-laminated timber (clt) shear walls: hygro-mechanical model validation and parametric analysis. Archives of Civil and Mechanical Engineering **22**(2), 1–18 (2022)

[59] Pei, S., van de Lindt, J.W., Barbosa, A.R., Berman, J.W., McDonnell, E., Daniel Dolan, J., Blomgren, H.-E., Zimmerman, R.B., Huang, D., Wichman, S.: Experimental seismic response of a resilient 2-story mass-timber building with post-tensioned rocking walls. Journal of Structural Engineering **145**(11), 04019120 (2019)

[60] Ajrab, J.J., Pekcan, G., Mander, J.B.: Rocking wall–frame structures with supplemental tendon systems. Journal of Structural Engineering **130**(6), 895–903 (2004)

[61] Sarti, F., Palermo, A., Pampanin, S.: Quasi-static cyclic testing of two-thirds scale unbonded posttensioned rocking dissipative timber walls. Journal of Structural Engineering **142**(4), 4015005 (2016)

[62] Fitzgerald, D., Miller, T.H., Sinha, A., Nairn, J.A.: Cross-laminated timber rocking walls with slip-friction connections. Engineering Structures **220**, 110973 (2020)

[63] Pei, S., Huang, D., Berman, J., Wichman, S.: Simplified dynamic model for post-tensioned cross-laminated timber rocking walls. Earthquake Engineering & Structural Dynamics **50**(3), 845–862 (2021)

[64] Huang, D., Pei, S., Busch, A.: Optimizing displacement-based seismic design of mass timber rocking walls using genetic algorithm. Engineering Structures **229**, 111603 (2021)

[65] Housner, G.W.: The behavior of inverted pendulum structures during earthquakes. Bulletin of the seismological society of America **53**(2), 403–417 (1963)

[66] Di Egidio, A., Alaggio, R., Aloisio, A., de Leo, A.M., Contento, A.,

Tursini, M.: Analytical and experimental investigation into the effectiveness of a pendulum dynamic absorber to protect rigid blocks from overturning. International Journal of Non-Linear Mechanics **115**, 1–10 (2019)

[67] Pagliaro, S., Aloisio, A., Alaggio, R., Di Egidio, A.: Rigid block coupled with a 2 dof system: Numerical and experimental investigation. Coupled systems mechanics **9**(6), 539–562 (2020)

[68] Di Egidio, A., Pagliaro, S., Fabrizio, C., de Leo, A.M.: Seismic performance of frame structures coupled with an external rocking wall. Engineering Structures **224**, 111207 (2020)

[69] Priestley, M.N., Sritharan, S., Conley, J.R., Pampanin, S.: Preliminary results and conclusions from the presss five-story precast concrete test building. PCI journal **44**(6), 42–67 (1999)

[70] Gibbons, J.D., Fielden, J.D.G.: Nonparametric Statistics: An Introduction vol. 90. Sage, ??? (1993)

[71] Strang, G.: Linear Algebra and Its Applications. Belmont, CA: Thomson, Brooks/Cole, ??? (2006)

[72] Goulet, J.-A.: Probabilistic Machine Learning for Civil Engineers. MIT Press, ??? (2020)

[73] Aloisio, A., Fragiacomo, M.: Reliability-based overstrength factors of cross-laminated timber shear walls for seismic design. Engineering Structures **228**, 111547 (2021)

[74] Ferreira, F., Moutinho, C., Cunha, Á., Caetano, E.: An artificial accelerogram generator code written in matlab. Engineering Reports **2**(3), 12129 (2020)

[75] Baker, J.W.: Efficient analytical fragility function fitting using dynamic structural analysis. Earthquake Spectra **31**(1), 579–599 (2015)

10 Appendix

The list of 41 Italian earthquake records with magnitude ranging between 5 and 6.5 is given in Tab. 9.

Table 9 List of earthquake recordings sorted from largest to smallest Peak Ground Acceleration (PGA).

No	**Year**	**Location (Italy)**	**Epicentral distance** [km]	**PGA** [g]	**Depth** [km]	**ML**	**MW**
1	2016	Norcia	11.0	**0.931**	9.2	6.1	6.5
2	2016	Accumoli	8.5	**0.851**	8.1	6.0	6.0
3	2009	Fossa	3.6	**0.652**	17.1	5.4	5.5
4	2009	L'aquila	4.9	**0.644**	8.3	5.9	6.1
5	2016	Visso	7.1	**0.638**	7.5	5.9	5.9
6	1976	Lusevra	6.2	**0.632**	6.8	6.1	5.9
7	2009	Montereale	7.9	**0.550**	9.4	5.3	5.4
8	2012	Medolla	9.3	**0.495**	8.1	5.8	6.0
9	1976	Lusevra	27.7	**0.346**	5.7	6.4	6.4
10	1976	Gemona del friuli	16.2	**0.342**	11.3	6.0	6.0
11	1976	Friuli Venezia Giulia	9.4	**0.322**	4.3	5.8	5.6
12	1980	Laviano	33.3	**0.314**	15.0	6.5	6.9
13	2016	Castel Sant'Angelo sul Nera	9.4	**0.295**	8.1	5.4	5.4
14	2009	L'Aquila	11.0	**0.294**	11.0	5.1	5.4
15	2017	Cagnano amiterno	10.8	**0.289**	9.5	5.1	5.0
16	2009	L'Aquila	7.4	**0.264**	9.0	5.0	5.0
17	2012	Finale Emilia	16.1	**0.259**	9.5	5.9	6.1
18	2012	San Possidonio	6.9	**0.252**	7.2	5.1	5.5
19	1976	Nimis	7.0	**0.241**	13.3	5.5	5.1
20	1977	Trasaghis	7.1	**0.238**	10.8	5.3	5.3
21	2013	Fivizzano	11.9	**0.227**	7.0	5.2	5.1
22	2012	San Felice sul Panaro	7.4	**0.205**	5.0	5.1	9.1
23	1984	Perugia	20.6	**0.201**	6.0	5.2	5.6
24	2016	Norcia	4.4	**0.191**	8.0	5.4	5.3
25	1997	Foligno	20.1	**0.184**	5.5	5.4	5.4
26	1997	Foligno	21.6	**0.184**	5.7	5.8	6.0
27	2001	Naturno	25.9	**0.167**		5.3	4.8
28	1984	Villetta Barrea	17.4	**0.158**	12.1	5.7	5.5
29	1997	Foligno	24.2	**0.152**	5.7	5.6	5.7
30	2009	Pizzoli	10.1	**0.148**	9.7	5.0	5.1
31	1984	Settefrati	10.1	**0.110**	20.5	5.9	5.9
32	2012	Berceto	67.4	**0.098**	72.4	5.2	5.0
33	1990	Potenza	29.0	**0.096**	10.0	5.2	5.8
34	1997	Sellano	4.1	**0.082**	4.8	5.1	5.2
35	1978	Bruzzano Zeffirio	9.2	**0.076**	5.0	5.3	5.2
36	2004	Vobarno	13.6	**0.072**	5.4	5.2	5.0
37	2012	Mirabello	20.4	**0.070**	3.4	5.1	5.2
38	2002	Bonefro	38.1	**0.057**	13.0	5.4	5.7
39	2018	Molise	22.3	**0.045**	19.6	5.2	5.1
40	2002	Casacalenda	46.1	**0.032**	10.0	5.3	5.7
41	2008	Neviano degli Arduini	47.6	**0.022**	22.9	5.2	5.5